



HAL
open science

Identification of montmorillonite particle edge orientations by atomic-force microscopy

Sergey Kraevsky, Christophe Tournassat, Marylène Vayer, Fabienne Warmont, Sylvain Grangeon, Brice F. Ngouana Wakou, Andrey G. Kalinichev

► To cite this version:

Sergey Kraevsky, Christophe Tournassat, Marylène Vayer, Fabienne Warmont, Sylvain Grangeon, et al.. Identification of montmorillonite particle edge orientations by atomic-force microscopy. Applied Clay Science, 2020, 186, 105442 (8 p.). 10.1016/j.clay.2020.105442 . insu-02476314

HAL Id: insu-02476314

<https://insu.hal.science/insu-02476314v1>

Submitted on 12 Feb 2020

HAL is a multi-disciplinary open access archive for the deposit and dissemination of scientific research documents, whether they are published or not. The documents may come from teaching and research institutions in France or abroad, or from public or private research centers.

L'archive ouverte pluridisciplinaire **HAL**, est destinée au dépôt et à la diffusion de documents scientifiques de niveau recherche, publiés ou non, émanant des établissements d'enseignement et de recherche français ou étrangers, des laboratoires publics ou privés.

1
2
3
4
5
6
7
8
9
10
11
12
13
14
15
16
17
18
19
20
21
22
23

**Identification of montmorillonite particle edge orientations by atomic-force
microscopy**

**Sergey V. Kraevsky^{1,2,3,4,*}, Christophe Tournassat^{2,5,6}, Marylène Vayer⁷,
Fabienne Warmont⁷, Sylvain Grangeon², Brice F. Ngouana Wakou¹,
and Andrey G. Kalinichev^{1,8}**

¹ Laboratoire SUBATECH (UMR 6457 - Institut Mines-Télécom Atlantique,
Université de Nantes, CNRS/IN2P3), 44307 Nantes, France

² BRGM, 3 avenue Claude Guillemin, 45060 Orléans, France

³ Kurchatov Institute - ITEP, 117218 Moscow, Russian Federation

⁴ Federal Research and Clinical Center of Physical-Chemical Medicine,
119435, Moscow, Russian Federation

⁵ Université d'Orléans – CNRS/INSU – BRGM, UMR 7327 Institut des Sciences de la Terre
d'Orléans, 45071 Orléans, France

⁶ Lawrence Berkeley National Laboratory, 1 Cyclotron Road, Berkeley, CA 94720, USA

⁷ ICMN-CNRS-Université d'Orléans, 1b rue de la Férollerie, 45071 Orléans Cedex 2, France

⁸ National Research University Higher School of Economics, Moscow, Russian Federation

*Corresponding author: Sergey V. Kraevsky (s.kraevsky@rcpcm.org)

24 **ABSTRACT**

25 Statistical information on the edge surface area and edge crystallographic orientation of clay
26 nanoparticle surfaces is essential for proper accounting of the protonation-deprotonation reactions
27 as a part of mechanistic surface complexation models. A combination of atomic-force microscopy
28 (AFM) measurements and molecular dynamics computer simulations made it possible to quantify
29 the relative contributions of the most frequently occurring montmorillonite edge surfaces to the
30 total edge surface area. Edge surfaces normal to the [110] and [010] crystallographic directions are
31 found to be the most abundant (~60% and ~20%, respectively), in agreement with previous
32 estimations.

33

34 **Keywords:** clay nanoparticles, montmorillonite, edges ratio, AFM, MD simulations

35

36 INTRODUCTION

37 The adsorption and resulting retardation of many contaminants by clay minerals make them
38 ideal for use in natural or engineered barrier systems (ANDRA, 2005; Gates et al. 2009; Marty et
39 al., 2010). The determination of a macroscopic retardation coefficient is a first step towards the
40 quantification of sorption and thus retardation of ions by mineral surfaces, but a sound mechanistic
41 understanding of the molecular-scale interaction between ions and surfaces is mandatory to the
42 building of reliable geochemical models (Tournassat et al., 2013; Borisover and Davis, 2015).
43 However, accurate mechanistic modeling of ion adsorption on clay mineral surfaces remains
44 challenging because of the diversity of adsorption sites on the basal and edge surfaces of clay
45 mineral particles (Churakov, 2006). The view that the acid-base properties of amphoteric groups at
46 the edge surfaces as well as the free energy of specific adsorption of cations (Ni^{2+} , UO_2^{2+} , *etc.*) are
47 dependent on the crystallographic orientation of the surface (Everett, 1998) is supported by *ab initio*
48 molecular dynamics (MD) computer simulations (Churakov, 2006; Liu et al., 2008, 2012, 2013,
49 2014, 2015a,b; Zhang et al., 2017), and the construction of mechanistic surface complexation
50 models (SCM) for clay minerals thus necessitates to have a statistical information on the edge
51 surface area and edge crystallographic orientation of clay mineral layer surfaces (Bourg et al.,
52 2007, Tournassat et al., 2016, Zhang et al., 2018). In the present study, we focused our efforts on
53 montmorillonite, *i.e.* the dioctahedral smectite of which the adsorption properties have been the
54 most studied in the literature.

55 Previous classical and *ab initio* molecular dynamics (MD) simulations of hydrated
56 montmorillonite edges suggested that the nanoparticle surfaces normal to the [110] crystallographic
57 direction may be significantly more stable than the surfaces normal to the [010] direction (Bickmore
58 et al, 2003; Churakov, 2006; Newton et al, 2015, 2016; Kwon and Newton, 2016). Cleavage
59 energies (ΔE) and corresponding Gibbs free energies (ΔG) for edge surfaces predicted by density
60 functional theory (DFT) are also in agreement with these findings. For example, Lavikainen et al.
61 (2015) calculated that the ratio of (110), (010) and (100) edge surfaces of pyrophyllite, an uncharged

62 clay mineral with a layer structure similar to montmorillonite, is 69%, 29%, and 2%, respectively,
63 while the (130) edge surface represents less than 1% of the total surface area. However,
64 montmorillonite layers exhibit significant differences with the pyrophyllite layers. First of all,
65 montmorillonite layers are negatively charged due to the presence of isomorphic substitutions in
66 their octahedral and tetrahedral sheets. Secondly, pyrophyllite has a trans-vacant layer structure,
67 while most montmorillonite samples have a cis-vacant layer structure (Tsipursky and Drits, 1984).
68 Hence, the relative proportions of different edge faces contributing to the total surface area of the
69 charged montmorillonite nanoparticles is still largely unknown.

70 Numerous recent atomic force microscopy (AFM) studies of different clays prove the
71 possibility to achieve a real atomic scale resolution of clay structures. For instance, Ferrage et al.
72 (2006) used X-ray and electron diffraction for the interpretation of their AFM atomic scale images.
73 Siretanu et al. (2016), studied surface defects of different clay materials, including montmorillonite,
74 and demonstrated that AFM can provide insights on the morphology and atomic scale structure of
75 clay layers.

76 At the same time, atomistic computer simulations have been already demonstrated to be
77 very insightful in interpreting the AFM images of hydrated mineral surfaces enabling one to clarify
78 the underlying imaging mechanism in the AFM experiments (Kobayashi et al., 2016; Umeda et al.,
79 2017; Reischl et al., 2019).

80 In the present work, we used AFM experiments for visualization and quantitative
81 characterization of the geometry and size distribution of montmorillonite particles, as well as for
82 reliable determination of the crystallographic orientation of their edges. Fourier peaks of the AFM-
83 images were then decoded using the insight from the atomistic computer simulations of the same
84 systems.

85

86 **MATERIALS AND METHODS**

87 **Clay mineral**

88 The Kunipia-P sample used in this study is a purified Na-montmorillonite produced by
89 Kunimine industries Co. Ltd., and which contains nearly 100% montmorillonite (Tachi and Yotsuji,
90 2014; Orucoglu et al. 2018). Kunipia-P montmorillonite was dispersed in deionized water at a solid
91 concentration of 0.01 g L⁻¹ and ultrasonicated for 10 min. A droplet of the dispersion was then
92 deposited on a freshly cleaved mica surface (purity grade V1, Ted Pella, Inc.) and dried overnight
93 in a desiccator.

94 **AFM samples preparation**

95 AFM measurements were carried out with samples mounted in dry- and fluid-cells using a
96 Dimension Icon AFM (Bruker) microscope in contact and peak force modes. The AFM images
97 were obtained in air with lateral force microscopy - friction data channel (Erlandsson et al., 1988;
98 Marti et al., 1990), using SNL-10 silicon nitride cantilevers (Bruker Inc.). The scan parameters
99 were: rate 5 Hz, angle 0, gains 0.3. Particles perimeter and surface area were estimated by
100 processing the AFM image using the FemtoScan (Filonov et al., 2001) and ImageJ
101 (<https://imagej.nih.gov>) softwares.

102 **Montmorillonite and muscovite structural models for MD simulations**

103 Classical MD simulations were performed with the LAMMPS software (Plimpton, 1995)
104 for a montmorillonite model that was built from an orthogonal pyrophyllite structure (Drits *et al.*,
105 2012), by randomly distributing Al/Si and Mg/Al isomorphic substitutions (Ngouana and
106 Kalinichev, 2014) in the tetrahedral and octahedral sheets of the layers, respectively. The simulation
107 supercell had dimensions of 4.1×3.6×10.5 nm³ and contained a montmorillonite clay particle
108 consisting of three T-O-T layers, each having 32 unit cells with the chemical composition
109 [Si_{7.75}Al_{0.25}][Al_{3.5}Mg_{0.5}]O₂₀(OH)₄Na_{0.75}(H₂O)₁₀, in which the layer charge of -0.75|e| per unit cell
110 was neutralized by Na⁺ ions. The layer-to-layer distance was selected and fixed to represent a
111 bilayer hydrate of Na-montmorillonite, with 10 H₂O/Na⁺ in each of the interlayers (Ngouana and

112 Kalinichev, 2014). The remaining volume of the simulation box was filled with 3280 H₂O
113 molecules to represent the interfacial liquid water at a density of 1 g/cm³, corresponding to ambient
114 conditions (Fig.1).

115 The muscovite model for classical MD simulations was built similarly from the same
116 orthogonal pyrophyllite structure (Drits *et al.*, 2012) by randomly distributing Al/Si isomorphic
117 substitutions in the tetrahedral sheets of the clay layers to achieve the chemical composition of
118 [Si₆Al₂][Al₄]O₂₀(OH)₄K₂] (see, e.g., Loganathan and Kalinichev, 2017). The simulation supercell
119 was a little shorter and had the dimensions of 4.1×3.6×8.5 nm³. The layer charge of -2.0|e| per unit
120 cell was neutralized by the corresponding number of interlayer and interfacial K⁺ ions and the rest
121 of the simulation cell was filled with 2960 H₂O molecules to achieve the liquid water density of
122 1 g/cm³, corresponding to ambient conditions (Fig.1).

123 **MD simulations parameters and procedure**

124 For both montmorillonite and muscovite models, the MD simulation protocol was the same.
125 The ClayFF force field (Cygan *et al.*, 2004) was used to calculate all the interatomic interactions
126 for each model. Periodic boundary conditions were applied and Ewald summation was used to
127 account for the long range electrostatic interactions in the system. The equations of atomic motion
128 were numerically integrated using a time step of 1 fs and each model was initially equilibrated
129 under ambient conditions ($T = 300$ K, $P = 1$ bar) during a 1 ns MD run in the *NPT* statistical
130 ensemble, followed by an additional 0.5 ns equilibration run in the *NVT* ensemble, before a 1 ns
131 *NVT* production MD run was started. The results of that equilibrium *NVT* MD run were then
132 statistically analyzed to extract various properties of the simulated systems.

133

134 **RESULTS AND DISCUSSION**

135 **Montmorillonite particle size and shape measurements**

136 A few individual particles of montmorillonite had a lath-like shape, which is typical for
137 mica crystals (Bauer et al., 2000; Güven, 2001) (Fig. 2). Some other montmorillonite particles had
138 fairly well defined straight boundaries, which suggests that they belonged to certain
139 crystallographic directions (Fig. 2 and 3).

140 To facilitate the calculation of the total edge surface area from the AFM images, the
141 concentration of montmorillonite was selected during sample preparation so that its particles
142 occupied the maximum area on the surface of the substrate but did not overlap each other (Fig. 3a).
143 Because most of the particles imaged by AFM were montmorillonite single layer particles (Fig. 3),
144 the edge specific surface area (SSA_{Edge}) was estimated from the computation of the perimeter to
145 area ratio (Tournassat et al., 2003, Yokohama et al., 2005, Le Forestier et al., 2010, Marty et al.,
146 2011, Reinholdt et al., 2013):

$$147 \quad SSA_{Edge} = \frac{Ph}{m} = \frac{Ph}{S_b h \rho} = \frac{P}{S_b} \times \frac{1}{\rho}$$

148 (2)

149 where P is the perimeter (m), h the height (m), S_b the basal surface area (m²) and ρ the density
150 (kg/m³) of the particle.

151 Montmorillonite particles do have a size distribution associated with the nature of
152 montmorillonite and the distribution of surface charge (Assemi et al., 2015). The range of values
153 of the P/S_b parameter calculated from more than 500 observed montmorillonite particles is shown
154 on Figure 3b. The strongest variations were observed for smaller particles with a basal area of less
155 than 0.1 μm^2 (about 20% of total) and the sub-range from particle to particle varied between 13-59
156 μm^{-1} . Approximately 60% of the particles had basal surface area in the range of 0.1-0.4 μm^2 , their
157 P/S_b parameter varied in the range of 8-13 μm^{-1} . The remaining 20% of the particles had a basal
158 area of more than 0.4 μm^2 , their P/S_b varies from 4-8 μm^{-1} .

159 A small but significant difference between the *dry*- and *fluid-cell* samples, $4.7 \pm 0.3 \text{ m}^2 \text{ g}^{-1}$
160 and $4.1 \pm 0.2 \text{ m}^2 \text{ g}^{-1}$, respectively, was observed. Very small particles may have been less strongly
161 attached to the mica substrate surface in the presence of liquid than larger particles. Consequently,
162 small particles with the highest perimeter to area ratio may have been lost. Assuming that the
163 density of montmorillonite is about $2.7\text{-}2.8 \text{ g cm}^{-3}$ (Tournassat and Appelo, 2011), SSA_{Edge} of
164 Kunipia-P particles was estimated to be $\sim 4.3 \pm 0.2 \text{ m}^2 \text{ g}^{-1}$, in good agreement with a previously
165 reported value for a similar material, $5.3 \text{ m}^2 \text{ g}^{-1}$ (Yokoyama et al., 2005).

166 **Crystallographic orientation of montmorillonite particle edge surfaces**

167 AFM images taken at high resolution evidenced structures with a period of $\sim 0.45 \text{ nm}$ when
168 scanning from top to bottom and $\sim 0.51 \text{ nm}$ when scanning from bottom to top. The interpretation
169 of such atomic-resolution AFM images should be done however with extreme care due to the
170 possibility of instrumental artefacts such as vibration noise or piezo ceramic hysteresis (e.g.,
171 Rodriguez-Fortun et al., 2011). To confirm that the periodic signal being analyzed actually
172 corresponds to the crystallographic structure of the particle and does not represent a periodic noise,
173 a series of control experiments with rotation of scanning direction were performed. Rotation of the
174 scanning angle led to the rotation of the observed periodic structure (Fig S1, more details on these
175 control experiments are provided in the supplementary materials to this paper). Thus, it was
176 concluded that the observed structure was due to the nature of the sample, and was not an artifact
177 of the piezoscanner.

178 In previous studies of muscovite (Kuwahara, 1999; Liu and Brown 1997, Leiro 2014), the
179 authors correlated the periodic structure images obtained by AFM with the structure of the surface
180 of the silica tetrahedral sheet. Ferrage et al. (2006) investigated the surface of talc crystals and also
181 brought it in correspondence with the periodic structure of the silica tetrahedral sheet. Teschke et
182 al. (2010) proposed that when performing the AFM scanning of clay mineral, the surface layer of
183 H_2O molecules should be taken into account in the interpretation of the signal. They indeed
184 observed, on a mica surface, a periodic structure of 0.45 nm that corresponded to the ice-Ih

185 (hexagonal) type, predicted by atomistic simulations (Odelius, 1997; Wang et al., 2005a, 2005b).
186 More detailed studies of the first several layers of water on the mica surface were performed using
187 oscillatory AFM techniques, which allow to construct force curves (Fukuma et al., 2005, 2010;
188 Kimura et al., 2010; Kobayashi, et al., 2013). Using MD simulations, Kobayashi et al. (2016)
189 investigated the interaction between a carbon nanotube (as an AFM probe) and a mica surface and
190 evaluated the contribution of various forces to such interaction, thus allowing them to construct a
191 density map of water molecules in the first and second hydration layers of the surface.

192 Hydration layers could be not taken in account if one identify reflections in the FFTs of high-
193 resolution electron microscopy study of montmorillonite (Drummy et al., 2005). Present AFM
194 experiments were performed under ambient relative humidity conditions of 20% and above. Under
195 these conditions, it is expected that approximately one to two monolayers of water are present at
196 clay surface (Cases et al., 1992).

197 In the present study, we performed MD simulations of hydrated mica and montmorillonite
198 surfaces for better understanding and interpretation of the nature of these periodic structures. The
199 ClayFF force field used in the simulations is primarily based on electrostatic interactions between
200 partial charges assigned to individual atoms and Lennard-Jones (12-6) function (Cygan et al.,
201 2004). Assuming that the main contribution to the interaction of the silicon nitride cantilever and
202 the surface of montmorillonite or mica is due to the electrostatic interactions (e.g., Gan, 2009), we
203 calculated the electrostatic potential induced by the distribution of atomic charges at every point in
204 space and compared the two-dimensional maps of the electrostatic potential along the clay surface
205 with the AFM images.

206 To calculate the surface electrostatic potential from MD simulations, the model supercell was
207 divided into a three-dimensional mesh with a resolution of $0.03 \times 0.03 \times 0.03 \text{ nm}^3$. For each element
208 of the mesh the electrostatic potential was computed according to:

$$U = \frac{1}{4\pi\epsilon} \sum_{k=1}^n \frac{q_k}{r_k} \quad (1)$$

where q_k – are the partial atomic charges of the ClayFF model (Cygan et al., 2004) and r_k – are the instantaneous distances between this particular element of the mesh and the charged atom. The calculation was performed every 10 ps along the equilibrium MD trajectory and the results were then time-averaged over the entire trajectory.

The averaging of the electrostatic potential calculated along the (001) plane at different distances from the solid/liquid interface over the entire MD-generated trajectory showed that, for mica, the K^+ on the surface are well localized and could contribute significantly to the AFM signal. This result is in agreement with previous findings using MD simulations (Kobayashi et al. 2016). On the contrary, on the surface of Na-montmorillonite, the averaged contribution of the Na^+ to the surface electrostatic potential is significantly blurred over the 1 ns time scale of the simulation (Fig. 4), and it is thus unlikely that Na^+ on the montmorillonite surface contribute significantly to the periodic patterns observed on AFM images.

Fast Fourier transform (FFT) of the periodic structures observed in high resolution the AFM images were further compared with the FFT of the calculated electrostatic potential maps of the first hydration layer obtained from MD simulations (Fig. 5). The FFT maps from the AFM images and the calculated electrostatic maps are qualitatively similar. Their main difference is in the absence of secondary peaks on the FFT maps from the AFM image due to experimental noise and/or structural disorder such as bending, slight variation in atomic positions, anisotropic displacement factors, vacancies and isomorphic substitutions. The most intense contributions to the FFT maps (dominant frequencies of the periodic signal) was assigned to the direction perpendicular to the [010] crystallographic direction with a periodicity of ~0.45 nm, ~0.23 nm (1/2 and 1/4 of the b crystallographic unit cell dimension, Fig. 5) and to the direction perpendicular to the [100] direction

233 with the periodicity of ~ 0.26 nm ($1/2$ of the a crystallographic unit cell dimension, Fig. 5).
 234 Consequently, we assumed that the bright reflex on the FFT of the AFM images with the periodicity
 235 of ~ 0.45 nm corresponded to the b direction of the particles.

236 To evaluate the relative abundances of different crystallographic edge surface orientations of
 237 montmorillonite nanoparticles, the AFM images were rotated in such a way that the edge
 238 perpendicular to the b direction was horizontal and became the reference vector for the angles
 239 characterizing the remaining edges (Fig. 6). Note that this method does not allow us to distinguish
 240 the edges perpendicular to the direction $[110]$ from the edges perpendicular to the opposite direction
 241 $[\bar{1}\bar{1}0]$ and the like.

242 In the case of a single monocrystalline particle, the crystallographic directions defining the
 243 orientations of its edge surfaces can be determined from AFM images on a nanometer scale (Fig. 6;
 244 supplementary materials).

245

246 **Table 1.** Calculated relative ratios of the edge lengths for a typical montmorillonite particle shown
 247 in Fig. 7, compared with the pyrophyllite particle edge ratios predicted by DFT
 248 calculations using two different methods marked ΔE (minimization of the cleavage
 249 energies) and ΔG (minimization of Gibbs free energies) (Lavikainen et al. 2015).

Edge surface normal to	Angle ($^{\circ}$)	Edge surface area ratios based on		
		AFM (this work)	DFT calculations from (Lavikainen et al. 2015)	
			ΔE	ΔG
[010]	0	0.20	0.33	0.29
[130]	30	0.09	0.00	0.00
[110]	60	0.56	0.61	0.69

[100]	90	0.03	0.06	0.02
unidentified	-	0.12	-	-

250

251 To determine the ratio of the edge lengths corresponding to each specific orientation, the
 252 results were averaged over a large number of measurements. Figure 7 shows the total histogram of
 253 the resulting distribution measured for individual 26 particles. The surfaces normal to the [110]
 254 direction was significantly more prevalent than the surfaces normal to the [010] direction (Fig. 7
 255 and Table 1), in good agreement with the predictions from recent atomistic simulations (Lavikainen
 256 at al. 2015, Newton et al., 2016).

257

258 CONCLUSIONS

259 The combination of atomic-force microscopy (AFM) measurements and molecular
 260 dynamics (MD) computer simulations enabled to identify and quantify the relative abundances of
 261 the most frequently occurring edge surfaces of montmorillonite. The total edge specific surface area
 262 was evaluated to be $SSA_{Edge} \sim 4.3 \pm 0.2 \text{ m}^2\text{g}^{-1}$. MD simulations were used to construct a 3D map of
 263 the electrostatic potential around montmorillonite particles placed on the surface of muscovite
 264 (mimicking the conditions of experimental observations). Fourier transformation of the calculated
 265 3D electrostatic potential maps made it possible to identify characteristic reflexes at $\sim 0.45 \text{ nm}$ and
 266 $\sim 0.23 \text{ nm}$ on the Fourier-transformed experimental AFM images. The reflex at $\sim 0.45 \text{ nm}$
 267 corresponds to the periodicity along the crystallographic b direction, while the reflex at $\sim 0.26 \text{ nm}$
 268 corresponds to the periodicity along the crystallographic a direction. The knowledge of the particle
 269 orientations made it possible to quantify the relative abundance of crystallographic directions of
 270 the montmorillonite edge surfaces. The edge surface normal to the [110] and [010] crystallographic
 271 directions were found to be the most abundant ($\sim 60\%$, $\sim 20\%$ respectively), in agreement with
 272 previously published estimations based on DFT simulations. According to our measurements, the

273 contribution of the edge surface normal to the [130] to the total SSA_{Edge} is equal to 10%, a value
274 which exceeds the prediction made using DFT simulations.

275

276 **ACKNOWLEDGMENTS**

277 This collaborative project between BRGM and SUBATECH was supported by the GL
278 CTEC Program funded by the French National Radioactive Waste Management Agency (ANDRA)
279 and by the industrial chair “Storage and Disposal of Radioactive Waste” at the Institut Mines-
280 Télécom Atlantique (funded by ANDRA, ORANO, and EDF). A.G.K. also acknowledges support
281 of the HSE University Basic Research Program in the framework of the Russian Academic
282 Excellence Project “5-100”.

283

284 **REFERENCES**

- 285 Assemi, S., Sharma, S., Tadjiki, S., Prisbrey, K., Ranville, J., Miller, J.D., 2015. Effect of Surface
286 Charge and Elemental Composition on the Swelling and Delamination of Montmorillonite
287 Nanoclays Using Sedimentation Field-flow Fractionation and Mass Spectroscopy. *Clays and*
288 *Clay Minerals* 63, 457–468. <https://doi.org/10.1346/CCMN.2015.0630604>
- 289 ANDRA, 2005, Evaluation of the feasibility of a geological repository in an argillaceous formation,
290 Dossier 2005, Argile – Synthesis, ANDRA, Châtenay-Malabry, 241pp.
- 291 Bauer, A., Velde, B., and Gaupp, R. (2016). Experimental constraints on illite crystal morphology.
292 *Clay Minerals* 35, 587–597.
- 293 Bickmore, B.R., Rosso, K.M., Nagy, K.L., Cygan, R.T., and Tadanier, C.J. (2003). Ab Initio
294 Determination of Edge Surface Structures for Dioctahedral 2:1 Phyllosilicates: Implications
295 for Acid-Base Reactivity. *Clays Clay Miner.* 51, 359–371.
- 296 Borisover, M. and Davis, J. A. Chapter 2 - Adsorption of inorganic and organic solutes by clay
297 minerals. In Tournassat, C.; Steefel, C. I.; Bourg, I. C. & Bergaya, F. (Eds.) *Natural and*
298 *Engineered Clay Barriers*, Elsevier, 2015, 6, 33-70
- 299 Bourg, I.C., Sposito, G., and Bourg, A.C.M. (2007). Modeling the acid–base surface chemistry of
300 montmorillonite. *Journal of Colloid and Interface Science* 312, 297–310.
- 301 Cases, J.M., Berend, I., Besson, G., Francois, M., Uriot, J.P., Thomas, F., Poirier, J.E. (1992).
302 Mechanism of adsorption and desorption of water vapor by homoionic montmorillonite. 1.
303 The sodium-exchanged form. *Langmuir* 8, 2730–2739. <https://doi.org/10.1021/la00047a025>
- 304 Churakov, S.V. (2006). Ab Initio Study of Sorption on Pyrophyllite: Structure and Acidity of the
305 Edge Sites. *J. Phys. Chem. B* 110, 4135–4146.
- 306 Cygan, R. T., Liang, J. J., Kalinichev, A. G. (2004). Molecular models of hydroxide, oxyhydroxide,
307 and clay phases and the development of a general force field. *J. Phys. Chem. B* 108, 1255–
308 1266.

309 Drits, V. A., Guggenheim, S., Zviagina, B. B., and Kogure, T. (2012). Structures of the 2:1 layers
310 of pyrophyllite and talc. *Clays Clay Miner.* 60, 574–587.

311 Erlandsson, R., Hadziioannou, G., Mate, C.M., McClelland, G.M., and Chiang, S. (1988). Atomic
312 scale friction between the muscovite mica cleavage plane and a tungsten tip. *J. Chem. Phys.*
313 89, 5190–5193.

314 Everett A. Jenne (1998). *Adsorption of Metals by Geomedia* (Elsevier).

315 Ferrage, E., Seine, G., Gaillot, A.-C., Petit, S., De Parseval, P., Boudet, A., Lanson, B., Ferret, J.,
316 and Martin, F. (2006). Structure of the {001} talc surface as seen by atomic force microscopy:
317 comparison with X-ray and electron diffraction results. *Eur. J. Mineral* 18, 483–491.

318 Filonov, A., Gavrilko, D., and Yaminsky, I. (2001). FemtoScan SPM Image damaging by the tip
319 during scanning. *Processing Software Manual*.

320 Fukuma, T., Kobayashi, K., Matsushige, K., and Yamada, H. (2005). True atomic resolution in
321 liquid by frequency-modulation atomic force microscopy. *Appl. Phys. Lett.* 87, 034101.

322 Fukuma Takeshi, Ueda Yasumasa, Yoshioka Shunsuke, and Asakawa Hitoshi (2010). Atomic-scale
323 distribution of water molecules at the mica-water interface visualized by three-dimensional
324 scanning force microscopy. *Phys. Rev. Lett* 104, 016101.

325 Le Forestier, L., Muller, F., Villieras, F., and Pelletier, M. (2010). Textural and hydration properties
326 of a synthetic montmorillonite compared with a natural Na-exchanged clay analogue. *Applied*
327 *Clay Science* 48, 18–25.

328 Gan, Y. (2009) Atomic and subnanometer resolution in ambient conditions by atomic force
329 microscopy. *Surface Science Reports* 64, 99-121.

330 Gates, W. P., Bouazza, A., Churchman, G. J. (2009). Bentonite clay keeps pollutants at bay.
331 *Elements*, 5, 105-110.

332 Güven, N. (2001). Mica structure and fibrous growth of illite. *Clays and Clay Minerals* 49, 189–
333 196.

334 Kimura, K., Ido, S., Oyabu, N., Kobayashi, K., Hirata, Y., Imai, T., and Yamada, H. (2010).
335 Visualizing water molecule distribution by atomic force microscopy. *J Chem Phys* *132*,
336 194705.

337 Kobayashi, K., Oyabu, N., Kimura, K., Ido, S., Suzuki, K., Imai, T., Tagami, K., Tsukada, M., and
338 Yamada, H. (2013). Visualization of hydration layers on muscovite mica in aqueous solution
339 by frequency-modulation atomic force microscopy. *J. Chem. Phys.* *138*, 184704.

340 Kobayashi, K., Liang, Y., Amano, K., Murata, S., Matsuoka, T., Takahashi, S., Nishi, N., and
341 Sakka, T. (2016). Molecular dynamics simulation of atomic force microscopy at the water–
342 muscovite interface: Hydration layer structure and force analysis. *Langmuir* *32*, 3608–3616.

343 Kuwahara, Y. (1999). Muscovite surface structure imaged by fluid contact mode AFM. *Phys Chem*
344 *Min* *26*, 198–205.

345 Kwon, K.D., and Newton, A.G. (2016). Structure and stability of pyrophyllite edge surfaces: Effect
346 of temperature and water chemical potential. *Geochim. Cosmochim. Acta* *190*, 100–114.

347 Lavikainen, L.P., Hirvi, J.T., Kasa, S., Schatz, T., and Pakkanen, T.A. (2015). Stability of
348 dioctahedral 2:1 phyllosilicate edge structures based on pyrophyllite models. *Theor Chem*
349 *Acc* *134*, 112.

350 Leiro, J.A., Torhola, M., and Laajalehto, K. (2017). The AFM method in studies of muscovite mica
351 and galena surfaces. *Journal of Physics and Chemistry of Solids* *100*, 40–44.

352 Liu, Z.H., and Brown, N.M.D. (1997). The influence of imaging conditions on the appearance of
353 lattice-resolved AFM images of mica surfaces. *J. Phys. D: Appl. Phys.* *30*, 2503–2508.

354 Liu, X., Lu, X., Wang, R., Zhou, H., and Xu, S. (2008). Surface complexes of acetate on edge
355 surfaces of 2:1 type phyllosilicate: Insights from density functional theory calculation.
356 *Geochimica et Cosmochimica Acta* *72*, 5896–5907.

357 Liu, X., Lu, X., Meijer, E.J., Wang, R., and Zhou, H. (2012). Atomic-scale structures of interfaces
358 between phyllosilicate edges and water. *Geochimica et Cosmochimica Acta* *81*, 56–68.

359 Liu, X., Lu, X., Sprik, M., Cheng, J., Meijer, E.J., and Wang, R. (2013). Acidity of edge surface
360 sites of montmorillonite and kaolinite. *Geochimica et Cosmochimica Acta* *117*, 180–190.

361 Liu, X., Cheng, J., Sprik, M., Lu, X., and Wang, R. (2014). Surface acidity of 2:1-type dioctahedral
362 clay minerals from first principles molecular dynamics simulations. *Geochimica et*
363 *Cosmochimica Acta* *140*, 410–417.

364 Liu, X., Cheng, J., Sprik, M., Lu, X., and Wang, R. (2015a). Interfacial structures and acidity of
365 edge surfaces of ferruginous smectites. *Geochimica et Cosmochimica Acta* *168*, 293–301.

366 Liu, X., Lu, X., Cheng, J., Sprik, M., and Wang, R. (2015b). Temperature dependence of interfacial
367 structures and acidity of clay edge surfaces. *Geochimica et Cosmochimica Acta* *160*, 91–99.

368 Loganathan, N. and Kalinichev, A. G., 2017. Quantifying the mechanisms of site-specific ion
369 exchange at an inhomogeneously charged surface: Case of Cs⁺/K⁺ on hydrated muscovite
370 mica. *Journal of Physical Chemistry C* *121*, 7829–7836.

371 Marti, O., Colchero, J., and Mlynek, J. (1990). Combined scanning force and friction microscopy
372 of mica. *Nanotechnology* *1*, 141.

373 Marty, N.C.M., Fritz, B., Clément, A., and Michau, N. (2010). Modelling the long term alteration
374 of the engineered bentonite barrier in an underground radioactive waste repository. *Applied*
375 *Clay Science* *47*, 82–90.

376 Marty, N.C.M., Cama, J., Sato, T., Chino, D., Villiéras, F., Razafitianamaharavo, A., Brendlé, J.,
377 Giffaut, E., Soler, J.M., Gaucher, E.C., et al. (2011). Dissolution kinetics of synthetic Na-
378 smectite. An integrated experimental approach. *Geochimica et Cosmochimica Acta* *75*,
379 5849–5864.

380 Newton, A.G., and Sposito, G. (2015). Molecular dynamics simulations of pyrophyllite edge
381 surfaces: Structure, surface energies, and solvent accessibility. *Clays Clay Miner* *63*, 277–
382 289.

383 Newton, A.G., Kwon, K.D., and Cheong, D.-K. (2016). Edge Structure of Montmorillonite from
384 Atomistic Simulations. *Minerals* *6*, 25.

385 Ngouana W., B.F., and Kalinichev, A.G. (2014). Structural arrangements of isomorphic
386 substitutions in smectites: Molecular simulation of the swelling properties, interlayer
387 structure, and dynamics of hydrated Cs–montmorillonite revisited with new clay models. *J.*
388 *Phys. Chem. C* *118*, 12758–12773.

389 Odelius, M., Bernasconi, M., and Parrinello, M. (1997). Two Dimensional Ice Adsorbed on Mica
390 Surface. *Phys. Rev. Lett.* *78*, 2855–2858.

391 Orucoglu, E., Tournassat, C., Robinet, J.-C., Madé, B., and Lundy, M. (2018). From experimental
392 variability to the sorption related retention parameters necessary for performance assessment
393 models for nuclear waste disposal systems: The example of Pb adsorption on clay minerals.
394 *Applied Clay Science* *163*, 20–32.

395 Plimpton, S. (1995). Fast Parallel Algorithms for Short-Range Molecular Dynamics. *Journal of*
396 *Computational Physics* *117*, 1–19.

397 Reinholdt, M.X., Hubert, F., Faurel, M., Tertre, E., Razafitianamaharavo, A., Francius, G., Prêt,
398 D., Petit, S., Béré, E., Pelletier, M., et al. (2013). Morphological properties of vermiculite
399 particles in size-selected fractions obtained by sonication. *Applied Clay Science* *77–78*, 18–
400 32.

401 Reischl, B., Raiteri, P., Gale, J.D., Rohl, A.L. (2019) Atomistic simulation of atomic force
402 microscopy imaging of hydration layers on calcite, dolomite, and magnesite surfaces.
403 *J. Phys. Chem. C* *123*, 14985-14992.

404 Rodriguez-Fortun, J.M., Orus, J., Alfonso, J., Buil, F., and Castellanos, J.A. (2011). Hysteresis in
405 piezoelectric actuators: Modeling and compensation. *IFAC Proceedings Vol. 44*, 5237–5242.

406 Siretanu, I., Ende, D. van den, and Mugele, F. (2016). Atomic structure and surface defects at
407 mineral-water interfaces probed by in situ atomic force microscopy. *Nanoscale* *8*, 8220–8227.

408 Tachi, Y., and Yotsuji, K. (2014). Diffusion and sorption of Cs⁺, Na⁺, Γ and HTO in compacted
409 sodium montmorillonite as a function of porewater salinity: Integrated sorption and diffusion
410 model. *Geochimica et Cosmochimica Acta* *132*, 75–93.

411 Teschke, O., Filho, J.F.V., and de Souza, E.F. (2010). Imaging two-dimensional ice-like structures
412 at room temperature. *Chemical Physics Letters* 485, 133–136.

413 Tournassat, C., and Appelo, C.A.J. (2011). Modelling approaches for anion-exclusion in compacted
414 Na-bentonite. *Geochimica et Cosmochimica Acta* 75, 3698–3710.

415 Tournassat, C., Davis, J.A., Chiaberge, C., Grangeon, S., and Bourg, I.C. (2016). Modeling the
416 acid–base properties of montmorillonite edge surfaces. *Environ. Sci. Technol.* 50, 13436–
417 13445.

418 Tournassat, C., Grangeon, S., Leroy, P., and Giffaut, E. (2013). Modeling specific pH dependent
419 sorption of divalent metals on montmorillonite surfaces. A review of pitfalls, recent
420 achievements and current challenges. *Am J Sci* 313, 395–451.

421 Tournassat, C., Neaman, A., Villiéras, F., Bosbach, D., and Charlet, L. (2003). Nanomorphology
422 of montmorillonite particles: Estimation of the clay edge sorption site density by low-pressure
423 gas adsorption and AFM observations. *American Mineralogist* 88, 1989–1995.

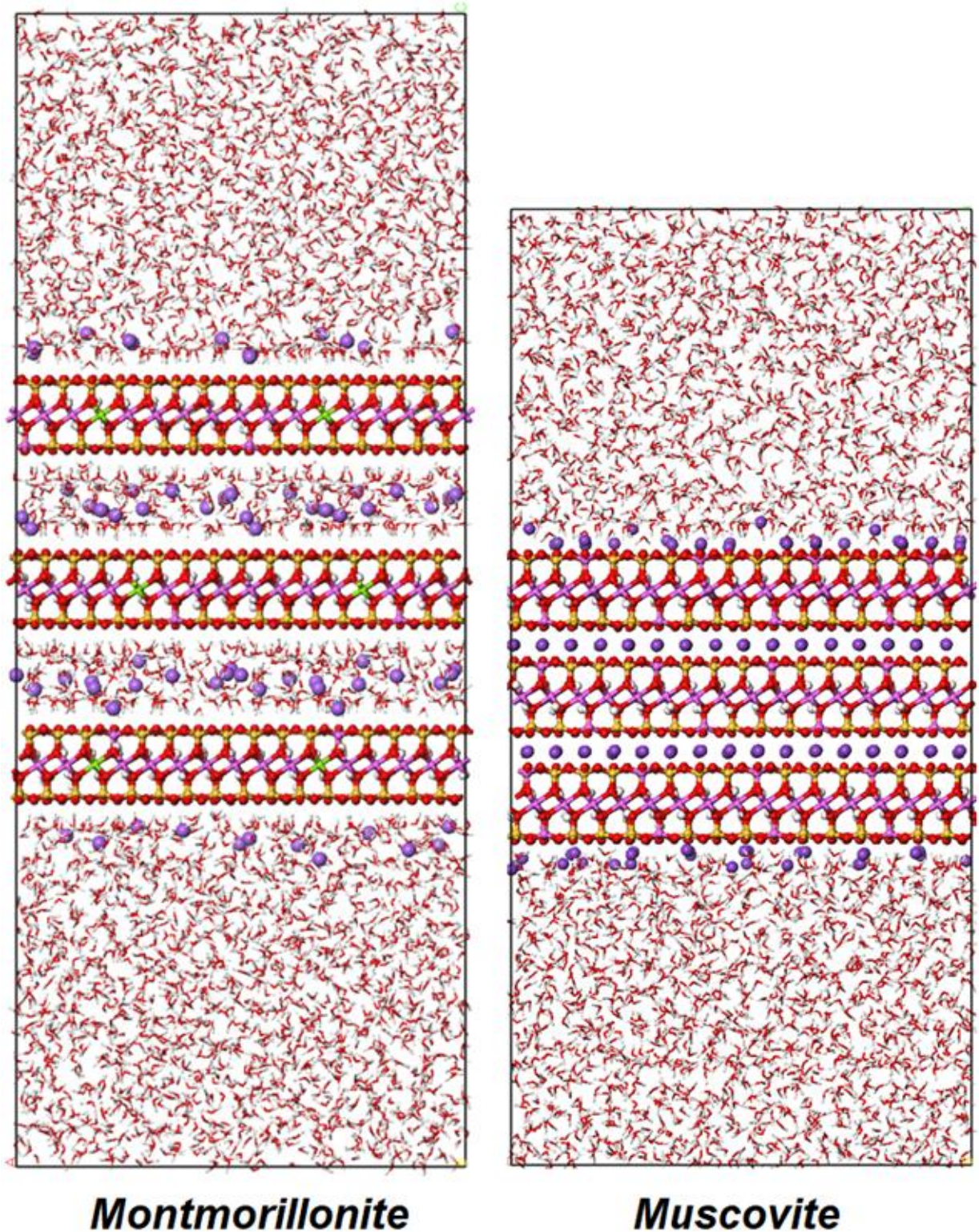
424 Tsipursky, S. I. and Drits, V. (1984) The distribution of octahedral cations in the 2:1 layers of
425 dioctahedral smectites studied by oblique-texture electron diffraction. *Clay Minerals*, 19,
426 177-193

427 Umeda, K., Zivanovic, L., Kobayashi, K., Ritala, J., Kominami, H., Spijker, P., Foster, A.S.,
428 Yamada, H. (2017). Atomic-resolution three-dimensional hydration structures on a
429 heterogeneously charged surface. *Nature Communications* 8, 2111.

430 Wang, J. W.; Kalinichev, A. G.; Kirkpatrick, R. J.; Cygan, R. T. (2005a) Structure, energetics, and
431 dynamics of water adsorbed on the muscovite (001) surface: A molecular dynamics
432 simulation. *Journal of Physical Chemistry B*, 109, 15893-15905.

433 Wang, J. W.; Kalinichev, A. G.; Kirkpatrick, R. J. (2005b) Structure and decompression melting of
434 a novel, high-pressure nanoconfined 2-D ice. *J. Phys. Chem. B*, 109, 14308-14313.

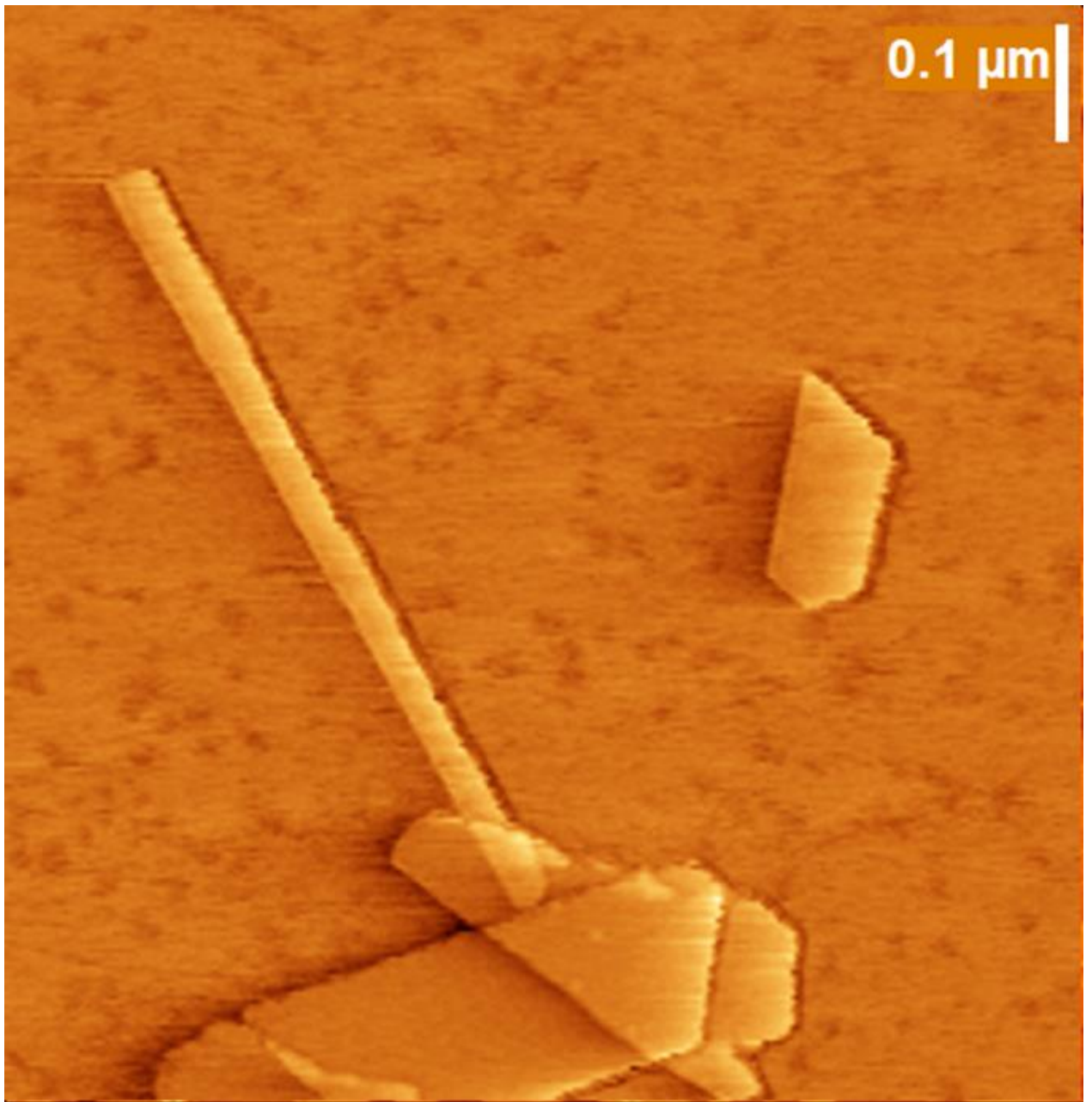
- 435 Yokoyama, S., Kuroda, M., and Sato, T. (2005). Atomic force microscopy study of montmorillonite
436 dissolution under highly alkaline conditions. *Clays Clay Miner* 53, 147–154.
- 437 Zhang, C., Liu, X., Lu, X., He, M., Meijer, E. J., and Wang, R. (2017) Surface complexation of
438 heavy metal cations on clay edges: insights from first principles molecular dynamics
439 simulation of Ni(II). *Geochimica et Cosmochimica Acta* 203, 54-68.
- 440 Zhang, C., Liu, X., Lu, X., and He, M. (2018) Complexation of heavy metal cations on clay edges
441 at elevated temperatures. *Chemical Geology* 479, 36-46.
- 442
- 443



445

446 Figure 1. General initial views of the simulation supercells of montmorillonite (left) and muscovite

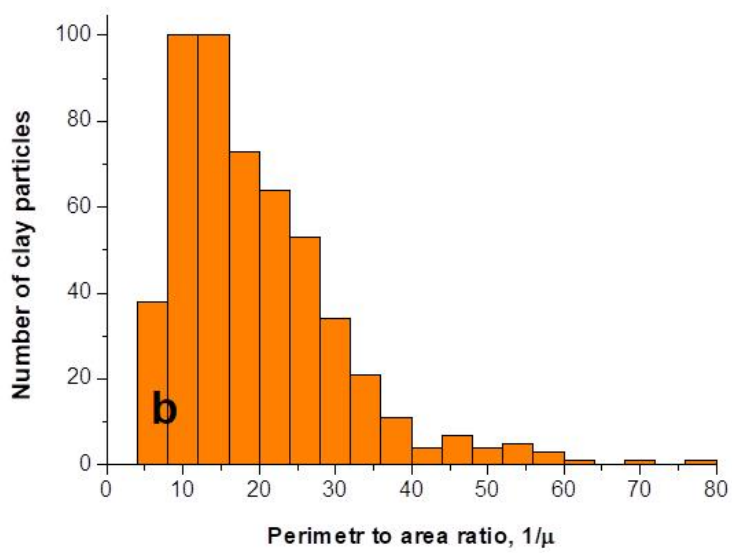
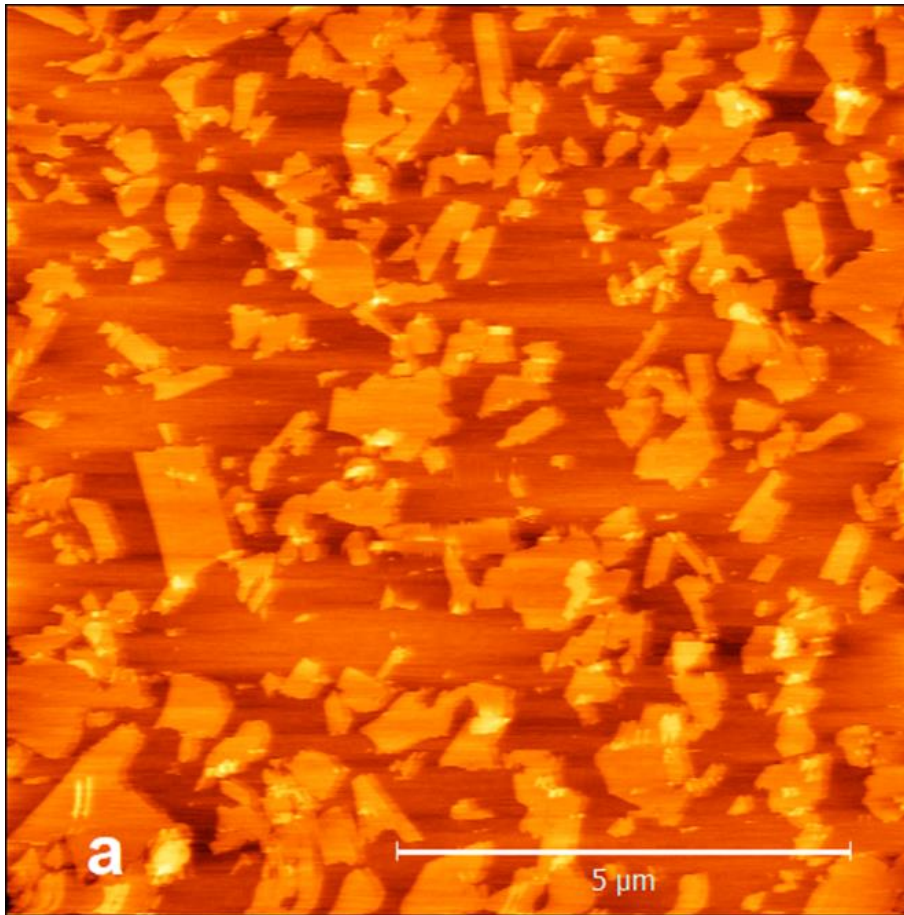
447 (right) used in the MD simulations.



448

449 Figure 2. Contact mode deflection AFM image of a clay particle with lath shape, and other particles

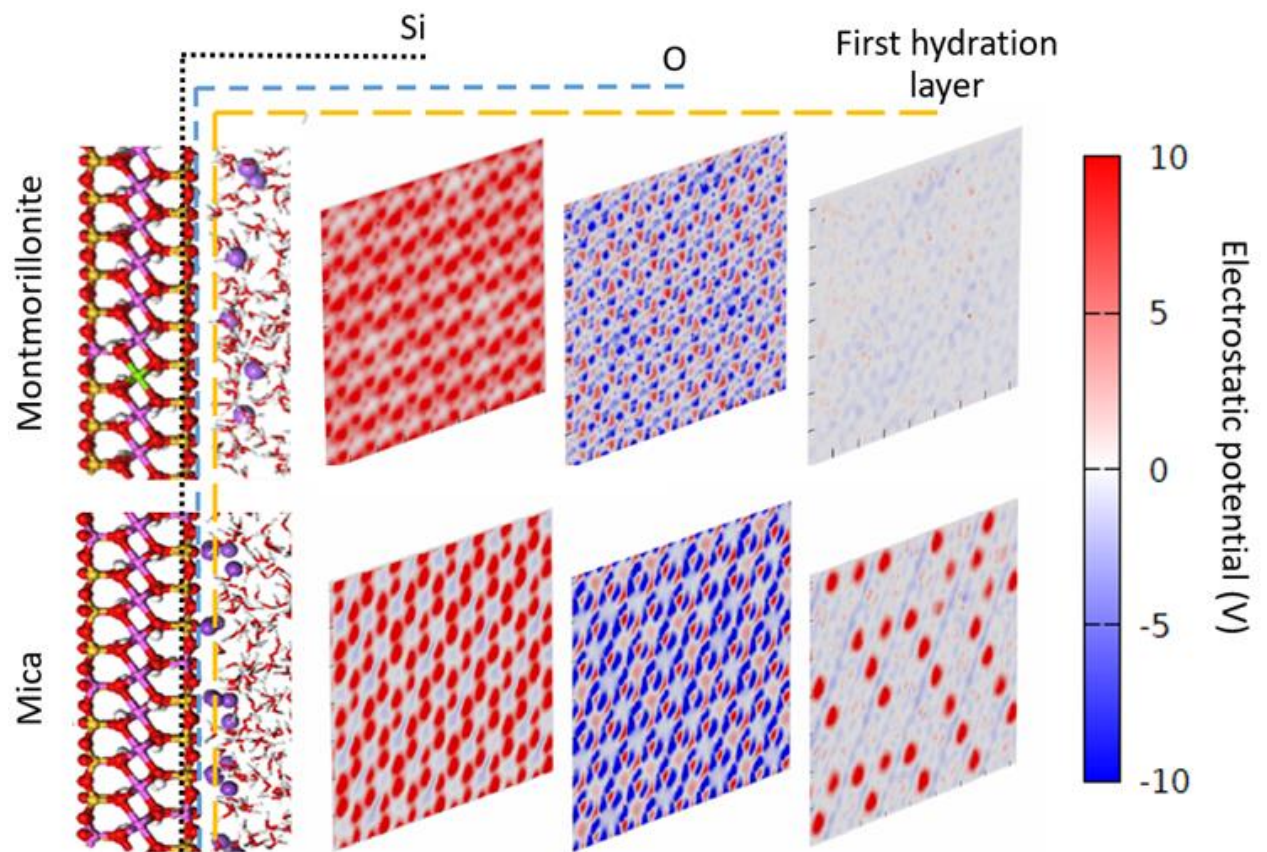
450 with well-defined straight boundaries.



451

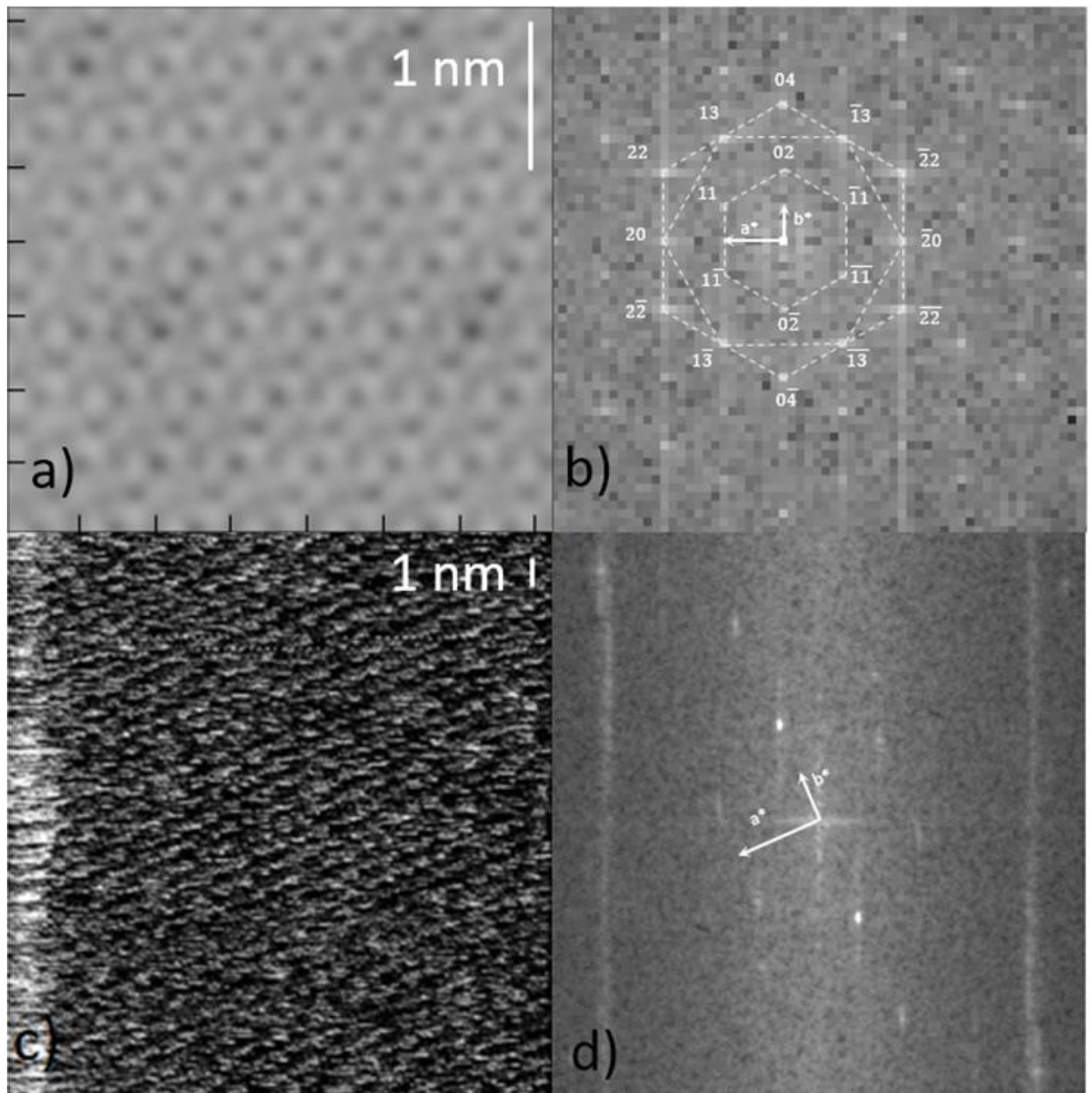
452 Figure 3. (a) Contact mode height AFM image of montmorillonite particles on the surface of
453 muscovite. (b) Histogram of perimeter-to-area ratio distribution of the measured montmorillonite
454 particles.

455



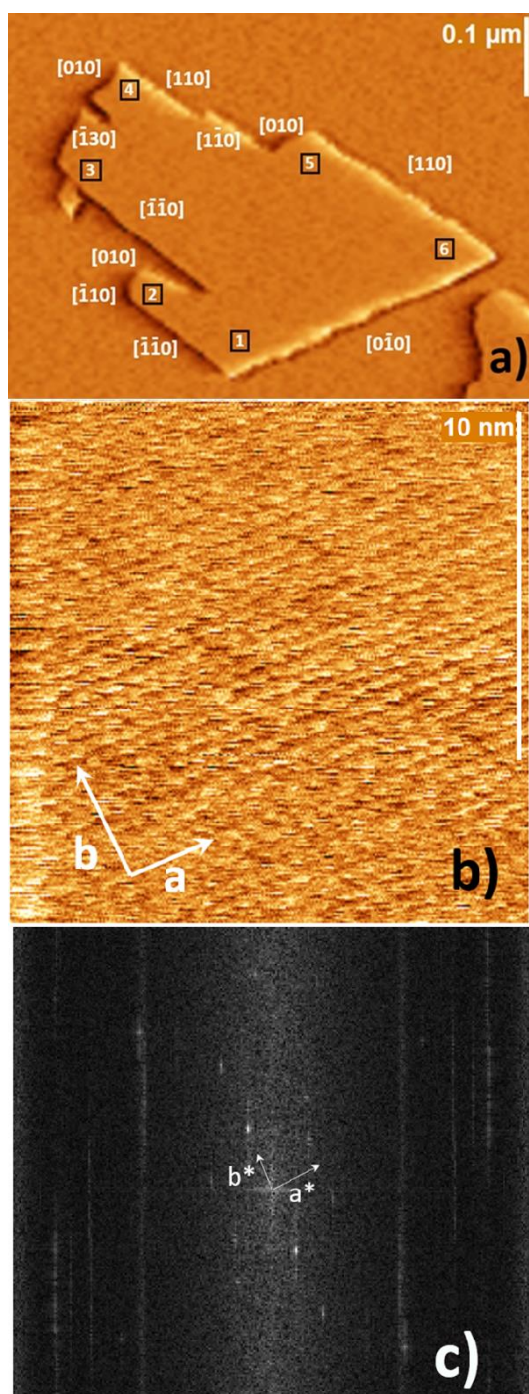
456

457 Figure 4. Maps of the time-averaged electrostatic potential (V) parallel to the (001) surface at
 458 different cross sections calculated from MD simulations. Maps drawn through the planes of time-
 459 averaged positions of the Si and O atoms of the clay show a honeycomb-like structure. The maps
 460 of electrostatic forces in the first hydrated surface, defined here as the plane 0.3 nm away from the
 461 plane of the surface O atoms, are much less ordered. In the case of montmorillonite, the honeycomb-
 462 like pattern is just barely distinguishable at the same color scale. In the case of the first hydration
 463 layer on the surface of the mica, the main contribution to the electrostatic forces is due to the
 464 absorbed K^+ counterions.



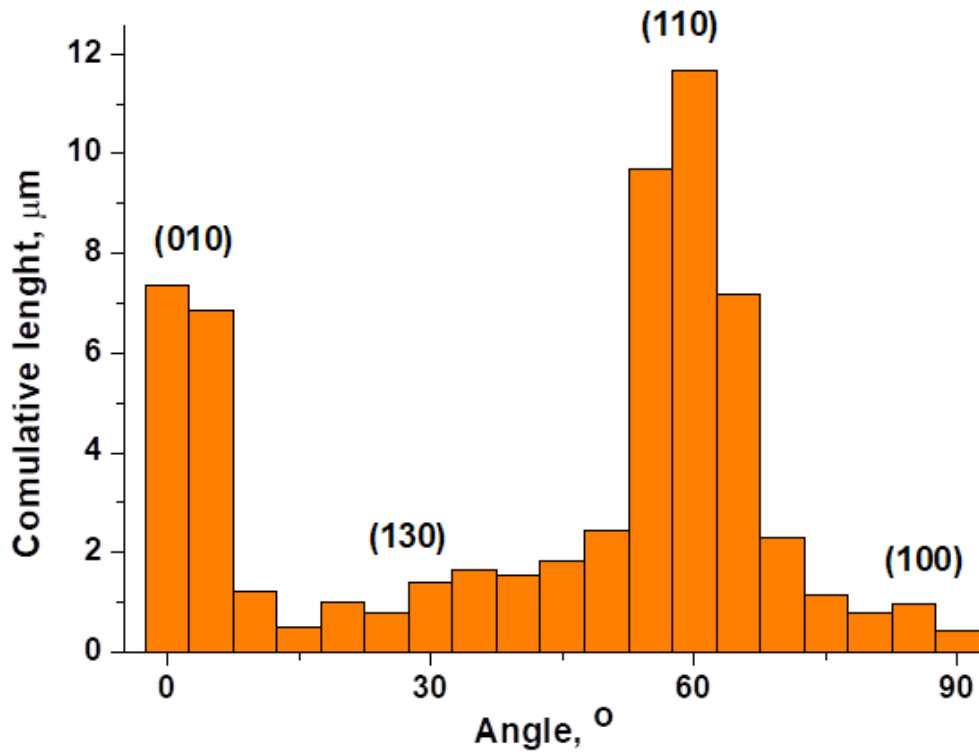
465

466 Figure 5. Electrostatic potential distribution into first hydration layer along the basal (001) surface
 467 of montmorillonite calculated from MD simulations (a) and its fast Fourier transform (b), compared
 468 with an friction mode AFM-image of the montmorillonite $15 \times 15 \text{ nm}^2$ surface (c) and its fast Fourier
 469 transform (d). In both FFT images one pair of reflections corresponding to a spatial periodicity of
 470 0.45 nm is brighter than the other two pairs. We are using this brightest pair to define the
 471 crystallographic direction b .



472

473 Figure 6. (a) AFM image of the montmorillonite particle; (b) atomic resolution AFM image
 474 captured on the square spot #1; (c) FFT of (b). The direction of vector b is chosen according to the
 475 brightest reflex with the 0.46 nm period, the sign of the vector is determined arbitrarily. To prove
 476 that the particle is, indeed, monocrystalline, several other atomic resolution images corresponding
 477 to spots #2-6 were obtained and provided as supplementary materials. The crystallographic indexes
 478 of the edge surfaces were defined by measuring the angle between the direction of the edge and the
 479 vector b .



480

481 Figure 7. Distribution histogram of montmorillonite particle edge surface orientations, with
 482 cumulative total lengths of the correspondingly oriented edges.

483

484

485

486

487

488

489

490

	Angle (°)	Edge surface area ratios based on
--	-----------	-----------------------------------

Edge surface normal to		AFM (this work)	DFT calculations from (Lavikainen et al. 2015)	
			ΔE	ΔG
[010]	0	0.20	0.33	0.29
[130]	30	0.09	0.00	0.00
[110]	60	0.56	0.61	0.69
[100]	90	0.03	0.06	0.02
unidentified	-	0.12	-	-

491

492 Table 1. Calculated relative ratios of the edge lengths for a typical montmorillonite particle shown
 493 in Fig. 7, compared with the pyrophyllite particle edge ratios predicted by DFT calculations using
 494 two different methods marked ΔE (minimization of the cleavage energies) and ΔG (minimization
 495 of Gibbs free energies) (Lavikainen et al., 2015).

496

497

498

499